

# SDSS galaxies with double-peaked emission lines: double starbursts or AGNs?

L.S. Pilyugin<sup>1</sup>, I.A. Zinchenko<sup>1</sup>, B. Cedrés<sup>2,3</sup>, J. Cepa<sup>2,3</sup>, A. Bongiovanni<sup>2,3</sup>, L. Mattsson<sup>4</sup>, J.M. Vílchez<sup>5</sup>

<sup>1</sup> Main Astronomical Observatory of National Academy of Sciences of Ukraine, 27 Zabolotnogo str., 03680 Kiev, Ukraine

<sup>2</sup> Instituto de Astrofísica de Canarias, C/ía Láctea S/N, 38200 La Laguna, Spain

<sup>3</sup> Departamento de Astrofísica, Universidad de La Laguna, E-38071 La Laguna, Tenerife, Spain

<sup>4</sup> Dark Cosmology Centre, Niels Bohr Institute, University of Copenhagen, Juliane Maries Vej 30, DK-2100, Copenhagen Ø, Denmark

<sup>5</sup> Instituto de Astrofísica de Andalucía, CSIC, Apdo, 3004, 18080 Granada, Spain

Accepted 2011 August 26. Received 2011 August 03; in original form 2011 March 23

## ABSTRACT

With the aim of investigating galaxies with two strong simultaneous starbursts, we have extracted a sample of galaxies with double-peaked emission lines in their global spectra from the SDSS spectral database. We then fitted the emission lines  $H\alpha$ ,  $H\beta$ ,  $[O\text{ III}]\lambda 5007$ ,  $[N\text{ II}]\lambda 6584$ ,  $[S\text{ II}]\lambda 6717$  and  $[S\text{ II}]\lambda 6731$  of 129 spectra by two Gaussians to separate the radiation of the two (blue and red) components. A more or less reliable decomposition of the all those emission lines have been found for 55 spectra. Using a standard BPT classification diagram, we have been able to divide the galaxies from our sample into two subsamples: Sample A consisting of 18 galaxies where both components belong to the photoionised class of objects, and Sample B containing 37 galaxies which show non-thermal ionisation (AGNs). We have examined the properties of the blue and red components, and found that the differences between radial velocities of components lie within  $200 - 400\text{ km s}^{-1}$  for galaxies of both subsamples. The equivalent number of ionising stars is in the range  $10^4 - 10^5$  O7V stars for each component in the galaxies of Sample A. We have estimated the oxygen and nitrogen abundances as well as the electron temperatures for each component using the recent NS-calibration and from global spectra for galaxies from Sample A using both the NS and ON-calibration. We have found that the global oxygen abundance is typically in between the measured abundances of individual components for our sample of galaxies, and that both calibrations provide consistent global abundances. Finally, we suggest the classical O/H – N/O diagram is used to test the reliability of the dividing lines between starburst-like objects and AGNs in the so-called BPT diagram.

**Key words:** galaxies: abundances – ISM: abundances – H II regions

## 1 INTRODUCTION

The study of starburst galaxies is very important for understanding both star formation and (chemical) evolution of galaxies. The Sloan Digital Sky Survey (SDSS, York et al. 2000) provides a very large database of spectra of galaxies, which has been used in many studies of the chemical evolution of galaxies (see, e.g., Kniazev et al. 2004; Izotov et al. 2004; Tremonti et al. 2004; Thuan et al. 2010; Pilyugin & Thuan 2007, 2011).

The SDSS spectra are obtained through 3-arcsec diameter fibers. At a redshift of  $z = 0.12$  (which is a mean value of the redshifts of galaxies considered at the present study), the projected aperture diameter is  $\sim 7$  kpc. This suggests that the SDSS spectra of the considered galaxies are closer to global spectra (composite nebulae that include multiple star clusters), rather than to spectra

of individual H II regions. In a typical case, many individual H II regions are distributed over the disc of a galaxy. Due to the rotation of galaxies, H II regions will have different radial velocities depending on the inclination of their host galaxy. One may expect that the emission line profile in the global SDSS spectra of such composite nebulae in distant galaxies can be described by a Gaussian which is wider than that for an individual H II region. If two strong starbursts take place in a galaxy and the giant H II regions associated with those starbursts make a dominant contribution to the radiation in the emission lines then one could expect double-peaked emission line profile in the global spectrum of a galaxy. While double-peaked emission lines have been extensively studied in AGN and radio galaxies, double starburst galaxies are yet unexplored. Those systems may induce errors in abundance determinations due to the mixing of two starburst events. Then, establishing the abundance

of those double-peaked starburst abundances as global systems, with respect to that defined by their components, will shed light on the role and possible impact of those double-peaked emission line galaxies on abundance determinations. To this aim, we have carried out a search for SDSS spectra of galaxies with double-peaked emission line profiles, revealing several hundreds of candidates where two strong starbursts can be observed simultaneously.

Here, we separate the radiation of two giant H II regions associated with two different starbursts by the fitting two Gaussians to the emission lines in the global spectra. We examine the properties of each component of these "binary starbursts": the electron density, the oxygen and nitrogen abundances, and the number of the ionising stars they contain. These objects provide also an additional possibility to test how representative abundances derived from global spectra are for the whole galaxies. Comparison between oxygen abundances in the blue and red components and global oxygen abundances will tell us something about the reliability of the abundances derived from global spectra. We test the reliability of global abundances by comparison of global abundances obtained using two recent strong-line calibrations as well.

Finally, we suggest to use the classical O/H – N/O diagram to test of the credibility of the dividing lines between the starburst-like objects and the AGNs in the Baldwin, Phillips & Terlevich (1981) (BPT) classification diagram.

The paper is organized as follows. Decomposition of the double-peaked emission line profiles in the global SDSS spectra and the selection of galaxies are described in Section 2. The general properties of the selected sample of galaxies are given in Section 3. The oxygen and nitrogen abundances and the electron temperatures derived for individual (blue or red) components and from global spectra are discussed in Section 4 and Section 5 gives a brief summary of the main results.

Throughout the paper, we will be using the following notations for the line fluxes,

$$R_2 = I_{[\text{O III}]\lambda 3727+\lambda 3729}/I_{\text{H}\beta}, \quad (1)$$

$$N_2 = I_{[\text{N II}]\lambda 6548+\lambda 6584}/I_{\text{H}\beta}, \quad (2)$$

$$S_2 = I_{[\text{S II}]\lambda 6717+\lambda 6731}/I_{\text{H}\beta}, \quad (3)$$

$$R_3 = I_{[\text{O III}]\lambda 4959+\lambda 5007}/I_{\text{H}\beta}. \quad (4)$$

The [O III]  $\lambda 5007$  and  $\lambda 4959$  lines originate from transitions from the same energy level, so their fluxes ratio is due only to the transition probability ratio which is close to 3 (Storey & Zeippen 2000). Hence, the value of  $R_3$  can be well approximated by

$$R_3 = 1.33 I_{[\text{O III}]\lambda 5007}/I_{\text{H}\beta}. \quad (5)$$

Similarly, the [N II]  $\lambda 6584$  and  $\lambda 6548$  lines also originate from transitions from the same energy level and the transition probability ratio for those lines is again close to 3 (Storey & Zeippen 2000). The value of  $N_2$  is therefore well approximated by

$$N_2 = 1.33 I_{[\text{N II}]\lambda 6584}/I_{\text{H}\beta}, \quad (6)$$

The electron temperatures  $t$  are given in units of  $10^4 \text{K}$ .

## 2 THE DATA

As the first step, we have extracted several hundred spectra of galaxies with double-peaked emission lines from the data release 7 (Abazajian et al. 2009) of the Sloan Digital Sky Survey (SDSS). In our previous work we have visually inspected SDSS spectra aiming

to search for spectra where the two auroral lines [O III]  $\lambda 4363$  and [N II]  $\lambda 5755$  can be detected simultaneously (Pilyugin et al. 2010). We have also collected spectra with double-peaked emission lines. Although we have considered all the SDSS DR7 spectra, we do not suggest our sample of SDSS spectra with double-peaked emission lines is exhaustive.

In order to separate the radiation of the blue and red components, we have fitted two Gaussians to the emission lines (H $\alpha$ , H $\beta$ , [O III]  $\lambda 5007$ , [N II]  $\lambda 6584$ , [S II]  $\lambda 6717$  and [S II]  $\lambda 6731$ ) in the extracted global spectra. The contribution of each individual component to the global flux have been derived as illustrated by the following example, concerning the H $\beta$  line. The continuum flux  $f_c$  is assumed to be constant between  $\lambda_a = 4836 \text{\AA}$  and  $\lambda_b = 4886 \text{\AA}$  (all spectra have been shifted to zero redshift). The line profiles of the blue and red components are approximated by Gaussians, i.e.,

$$f(\lambda) = F \frac{1}{\sqrt{2\pi}\sigma} e^{-(\lambda-\lambda_0)^2/2\sigma^2} \quad (7)$$

where  $\lambda_0$  is the central line wavelength,  $\sigma$  is the width of the line, and  $F$  is the flux in the emission line. Thus, the total flux at a fixed value of  $\lambda$  is given by the expression

$$f(\lambda) = f_{\text{H}\beta, \text{blue}}(\lambda) + f_{\text{H}\beta, \text{red}}(\lambda) + f_c(\lambda). \quad (8)$$

For the Gaussian fitting, we have used the robust non-linear least squares curve fitting package MPFIT<sup>1</sup> described in Markwardt (2009). MPFIT works much faster than a "brute-force" approach, but in some cases it may only find a local minimum. To avoid this, we calculated a set of best-fit parameters using MPFIT. We have considered  $\Delta\lambda = \lambda_0^{\text{red}} - \lambda_0^{\text{blue}}$  on the interval corresponding to differences between radial velocities of the blue and red components from 120 to 600  $\text{km s}^{-1}$ . This range was divided into 160 intervals  $\Delta\lambda_i$  with step 3  $\text{km s}^{-1}$ . The best-fit parameters for every interval of  $\Delta\lambda_i$  are derived by finding the minimum of the mean difference,

$$\epsilon = \sqrt{\frac{1}{n} \sum_{k=1}^{k=n} (f(\lambda_k) - f^{\text{obs}}(\lambda_k))^2}, \quad (9)$$

between the measured flux  $f^{\text{obs}}(\lambda_k)$  and the flux  $f(\lambda_k)$  given by Eq.(8) on the wavelength interval between  $\lambda_a$  and  $\lambda_b$ . The "true" values of  $F(\text{H}\beta, \text{blue})$ ,  $\lambda_0(\text{H}\beta, \text{blue})$ ,  $\sigma(\text{H}\beta, \text{blue})$ ,  $F(\text{H}\beta, \text{red})$ ,  $\lambda_0(\text{H}\beta, \text{red})$ ,  $\sigma(\text{H}\beta, \text{red})$  are then selected by comparing the minimum values of  $\epsilon_i$  for different intervals of  $\Delta\lambda_i$ . In other words, we have used a two-step procedure to obtain the best-fit parameters.

The fit to the [O III]  $\lambda 5007$  line is obtained using the wavelength interval from  $\lambda_a = 4982 \text{\AA}$  to  $\lambda_b = 5032 \text{\AA}$ . The continuum flux  $f_c$  is assumed to be constant between  $\lambda_a = 6523 \text{\AA}$  and  $\lambda_b = 6608 \text{\AA}$  in fitting of the H $\alpha$  and [N II]  $\lambda 6584$  lines, and between  $\lambda_a = 6690 \text{\AA}$  and  $\lambda_b = 6760 \text{\AA}$  in fitting of the [S II]  $\lambda 6717$  and [S II]  $\lambda 6731$  lines. The fits to the H $\alpha$ , H $\beta$ , [O III]  $\lambda 5007$ , [N II]  $\lambda 6584$ , [S II]  $\lambda 6717$  and [S II]  $\lambda 6731$  lines in the spectra (spSpec 280 51612 635) of the SDSS object J112655.58+004047.0 are shown in Fig. 1.

We have found 129 spectra where a double-Gaussian fit can be obtained for each emission line. Unfortunately the value of the parameter  $\epsilon$  given by Eq.(9) cannot serve as an effective criterion for selecting spectra with reliable decompositions. First of all, the value of  $\epsilon$  is a measure of the quality of the double-Gaussian fit to the global line profiles rather than a measure of the quality of the decomposition. In addition, the observed double-peaked line profiles are covered by about ten wavelength points only at the SDSS

<sup>1</sup> <http://purl.com/net/mpfit>

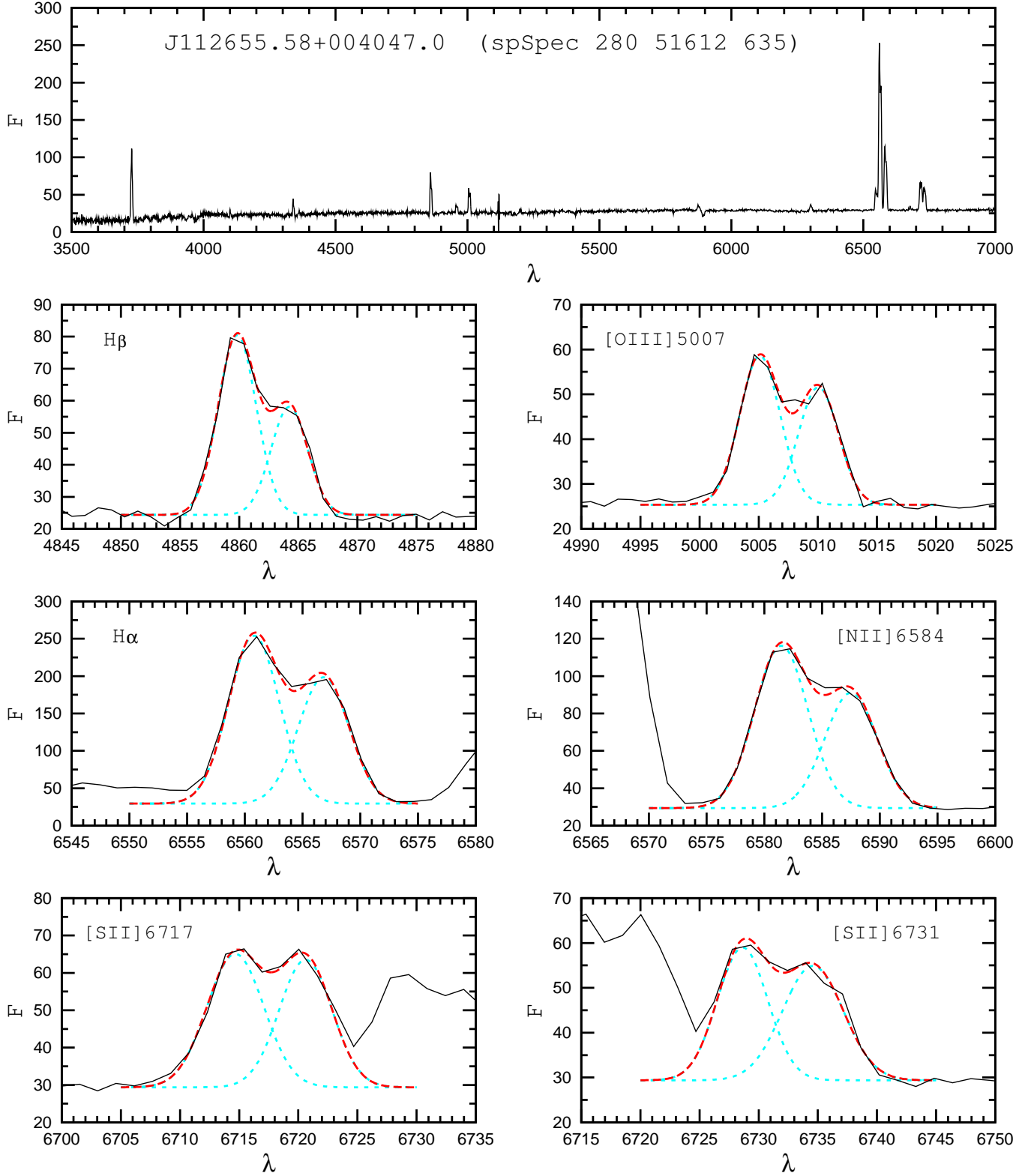


**Figure 1.** The observed spectrum of the SDSS object J112655.58+004047.0 (spSpec 280 51612 635) and double-Gaussian fits to the emission lines  $H\beta$ ,  $[OIII]\lambda 5007$ ,  $H\alpha$ ,  $[NII]\lambda 6584$ ,  $[SII]\lambda 6717$  and  $[SII]\lambda 6731$ . The solid line is the observed line profile. The long dashed (blue) lines are the profiles of the blue and red components, respectively, and the short dashed (red) line is the sum of the blue and red components. (A color version of this figure is available in the online version.)

spectroscopic resolution. Hence, the value of  $\epsilon$  may be affected significantly by the noise from just one data point. Therefore we have selected spectra where the decomposition of the blue and red components for each emission line seem to be reliable, based upon visual inspection of the double-Gaussian fits (how well a double-peak is seen in each emission line), taking into account the limited quality of the SDSS spectra. Our final list contains 55 spectra. Certainly, our selection is somewhat subjective, but as for the spectra excluded from further consideration here, the only lines that cannot be reliably decomposed into two components are [S II] $\lambda$ 6717 or/and [S II] $\lambda$ 6731. The other lines can be fitted rather well by two Gaussians. Even if the [S II] $\lambda$ 6717 and [S II] $\lambda$ 6731 lines will not be used as separate lines in the most part of this study, we have used the fits to these lines as a test of the robustness of the sample.

Since measurements of the [N II] $\lambda$ 6584 and [O III] $\lambda$ 5007 lines are more reliable than those of the [N II] $\lambda$ 6548 and [O II] $\lambda$ 4959 lines, we have used Eq.(6) to obtain the value of  $N_2$  and Eq.(5) to determine the value of  $R_3$ .

The measured emission fluxes  $F$  have been corrected for interstellar reddening. We have obtained the extinction coefficient  $C(H\beta)$  using the theoretical  $H\alpha$  to  $H\beta$  ratio ( $= 2.86$ ) and the analytical approximation to the Whitford interstellar reddening law by Izotov, Thuan & Lipovetsky (1994).

The redshift  $z$  and stellar mass  $M_S$  of each galaxy were taken from the MPA/JHU catalogs<sup>2</sup>. The techniques used to construct the catalogues are described in Brinchmann et al. (2004); Tremonti et al. (2004) and other publications of those authors.

### 3 GENERAL PROPERTIES OF THE SELECTED STARBURSTS

#### 3.1 BPT classification diagram

The intensities of strong, easily measured lines can be used to separate different types of emission-line objects according to their main excitation mechanism (i.e. starburst or AGN). Baldwin, Phillips & Terlevich (1981) proposed a diagram (BPT classification diagram) where the excitation properties of H II regions are studied by plotting the low-excitation [N II] $\lambda$ 6584/ $H\alpha$  line ratio against the high-excitation [O III] $\lambda$ 5007/ $H\beta$  line ratio. Using the BPT classification diagram, we have divided all galaxies from our sample into two subsamples. The first subsample (A) consists of 18 galaxies where both components (blue and red) are starburst like objects. The galaxies in Sample A are listed in Table 1. The second subsample (B) contains 37 galaxies where one or both components show non-thermal ionisation (here referred to as AGNs). It should be noted that all components, in all galaxies, in our sample have narrow lines regardless of their positions in the [N II] $\lambda$ 6584/ $H\alpha$  versus [O III] $\lambda$ 5007/ $H\beta$  diagram.

The theoretical  $H\alpha$ -to- $H\beta$  ratio for thermally photoionised nebulae has been used for de-reddening of measured emission lines in both subsamples. The application of the same de-reddening algorithm to all objects can be justified as follows. The parameters which are dependent on the absolute fluxes are analysed in the present study only for the starburst like objects (where this de-reddening algorithm is correct). As for the AGNs, this de-reddening algorithm can introduce an appreciable error in the de-reddened line intensities. However the de-reddened line intensities in the

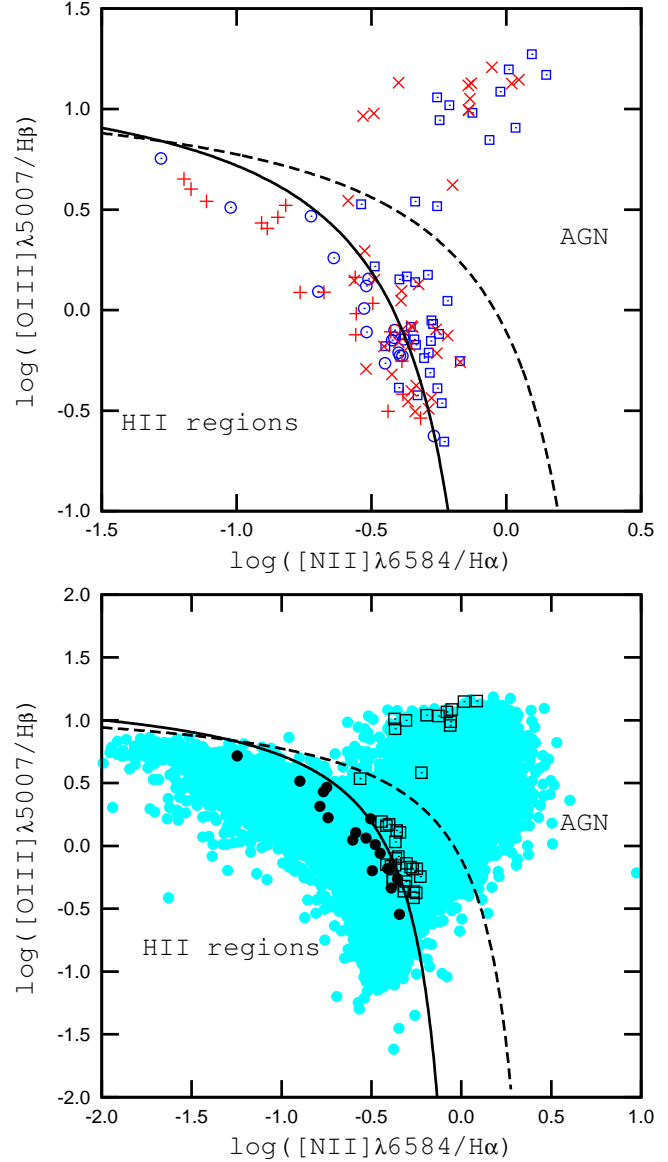


**Figure 2.** The [N II] $\lambda$ 6584/ $H\alpha$  versus [O III] $\lambda$ 5007/ $H\beta$  diagram. *Upper panel.* The open (blue) circles are the blue components and the (red) plus signs are the red components of the photoionised objects. The open (blue) squares are the blue components and the (red) crosses are the red components of the AGNs. The solid line separates objects with H II spectra from those containing an AGN according to Kauffmann et al. (2003), while the dashed line is the same according to Kewley et al. (2001). *Lower panel.* The gray (light-blue) filled circles show a large sample of emission-line SDSS galaxies from Thuan et al. (2010). The dark (black) filled circles show our sample of SDSS galaxies with double-peaked emission lines (global spectra, sum of blue and red components). (A color version of this figure is available in the online version.)

AGNs serve only for classification of those objects. The wavelengths of the [N II] $\lambda$ 6584 and  $H\alpha$  lines (as well [O III] $\lambda$ 5007 and  $H\beta$ ) are very similar and, consequently, the [N II] $\lambda$ 6584/ $H\alpha$ - and [O III] $\lambda$ 5007/ $H\beta$ -line ratios are not that sensitive to the de-reddening algorithm. Therefore, the adopted de-reddening algorithm does not result in a significant shift of the position of the object in the [N II] $\lambda$ 6584/ $H\alpha$  versus [O III] $\lambda$ 5007/ $H\beta$  diagram and is not likely to result in misclassification of objects.

The [N II] $\lambda$ 6584/ $H\alpha$  versus [O III] $\lambda$ 5007/ $H\beta$  diagram is shown

<sup>2</sup> The catalogs are available at <http://www.mpa-garching.mpg.de/SDSS/>

**Table 1.** Oxygen and nitrogen abundances and electron temperatures of individual components as well global values of Sample A.

SDSS number <sup>a</sup>	Spectrum number <sup>b</sup>	$12+\log(\text{O}/\text{H})_{\text{NS}}^{\text{blue}}$	$12+\log(\text{O}/\text{H})_{\text{NS}}^{\text{red}}$	$12+\log(\text{N}/\text{H})_{\text{NS}}^{\text{blue}}$	$12+\log(\text{N}/\text{H})_{\text{NS}}^{\text{red}}$	$t_{\text{NS}}^{\text{blue}}$	$t_{\text{NS}}^{\text{red}}$
		$12+\log(\text{O}/\text{H})_{\text{NS}}^{\text{glob}}$	$12+\log(\text{O}/\text{H})_{\text{ON}}^{\text{glob}}$	$12+\log(\text{N}/\text{H})_{\text{NS}}^{\text{glob}}$	$12+\log(\text{N}/\text{H})_{\text{ON}}^{\text{glob}}$	$t_{\text{NS}}^{\text{glob}}$	$t_{\text{ON}}^{\text{glob}}$
J015847.30-101802.7	665 52168 018	8.41	8.45	7.44	7.37	0.89	0.87
		8.43	8.45	7.41	7.45	0.88	0.86
J084845.58+542329.1	446 51899 595	8.47	8.24	7.69	6.85	0.80	1.06
		8.41	8.44	7.47	7.55	0.90	0.87
J091911.35+531424.0	553 51999 639	8.48	8.50	7.67	7.57	0.80	0.79
		8.49	8.46	7.63	7.46	0.80	0.83
J103007.07+412353.5	1360 53033 186	8.30	8.41	6.95	7.15	1.00	0.96
		8.37	8.42	7.07	7.25	0.97	0.95
J103404.17+061210.2	999 52636 150	8.22	8.16	6.85	6.71	1.09	1.12
		8.20	8.24	6.77	6.89	1.11	1.09
J103822.61+505814.7	1009 52644 042	8.48	8.42	7.70	7.47	0.80	0.87
		8.45	8.45	7.59	7.55	0.83	0.84
J104137.27+103252.0	1600 53090 020	8.52	8.61	7.98	7.97	0.74	0.69
		8.57	8.57	7.99	7.97	0.71	0.72
J112655.58+004047.0	280 51612 635	8.49	8.42	7.73	7.53	0.78	0.86
		8.46	8.44	7.64	7.55	0.82	0.83
J113122.19-005606.4	281 51614 007	8.41	8.37	7.47	7.20	0.89	0.93
		8.39	8.41	7.33	7.36	0.91	0.89
J113413.84+533601.2	1014 52707 096	8.41	8.15	7.31	6.70	0.92	1.12
		8.41	8.45	7.15	7.23	0.94	0.95
J113515.65+234606.0	2501 54084 010	8.40	8.32	7.12	6.93	0.87	0.99
		8.39	8.45	7.09	7.18	0.91	0.90
J113835.63+281801.1	2220 53795 089	8.41	8.33	7.42	6.95	0.89	0.90
		8.41	8.41	7.32	7.26	0.90	0.90
J114234.66-030527.9	329 52056 320	8.42	8.33	7.38	6.97	0.87	0.97
		8.37	8.43	7.06	7.13	0.93	0.93
J124844.42+250522.6	2661 54505 412	8.43	8.55	7.59	8.01	0.83	0.72
		8.47	8.44	7.73	7.58	0.80	0.82
J132253.24+585942.2	959 52411 397	8.46	8.54	7.64	7.86	0.82	0.73
		8.50	8.47	7.76	7.59	0.77	0.80
J141439.58+033601.8	583 52055 137	8.38	8.47	7.44	7.66	0.89	0.80
		8.42	8.44	7.54	7.56	0.84	0.83
J142504.46+050556.7	584 52049 571	8.45	8.43	7.63	7.44	0.82	0.88
		8.44	8.42	7.54	7.45	0.85	0.87
J161555.12+420624.5	1171 52753 376	8.51	8.38	7.40	7.08	0.89	0.96
		8.48	8.50	7.33	7.45	0.91	0.90

<sup>a</sup> The objects are listed in order of right ascension.<sup>b</sup> The spectrum number is composed of the SDSS plate number, the modified Julian date of the observation, and the number of the fiber on the plate.

in Fig. 2. The upper panel shows data for individual components. The open (blue) circles are the blue components and the (red) plus signs are the red components of the photoionised objects, while the open (blue) squares are the blue components and the (red) crosses are the red components of the AGNs. The solid line represents the equation

$$\log([\text{O III}]\lambda 5007/\text{H}\beta) = \frac{0.61}{\log([\text{N II}]\lambda 6584/\text{H}\alpha) - 0.05} + 1.3, \quad (10)$$

which separates objects with H II spectra from those containing an AGN (Kauffmann et al. 2003). The long-dashed separation line is the equation

$$\log([\text{O III}]\lambda 5007/\text{H}\beta) = \frac{0.61}{\log([\text{N II}]\lambda 6584/\text{H}\alpha) - 0.47} + 1.19, \quad (11)$$

from Kewley et al. (2001). The lower panel in Fig. 2 shows the global data. The gray (in the printed version – light-blue in the colour version) filled circles show a large sample of SDSS emission-line galaxies from Thuan et al. (2010). The dark (black)

filled circles show our sample of SDSS galaxies with double-peaked emission lines (global spectra, sum of blue and red components). The lines are the same as in the upper panel. We choose here to use the separation line from Kauffmann et al. (2003) (see below, Section 4).

Fig. 2 shows that in a majority cases either both components belong to starburst-like objects or to double-peaked AGNs. There seems to be a strong selection effect. Indeed the requirement that a reliable double-Gaussian fit can be obtained for each of the emission lines is satisfied for spectra with SDSS resolution only in cases when the contributions of the blue and red components are similar. As a result, our sample contains galaxies with similar  $[\text{N II}]\lambda 6584/\text{H}\alpha$ - and  $[\text{O III}]\lambda 5007/\text{H}\beta$ -fluxes for both components. Consequently, both components lie close to each other in the  $[\text{N II}]\lambda 6584/\text{H}\alpha$  versus  $[\text{O III}]\lambda 5007/\text{H}\beta$  diagram.

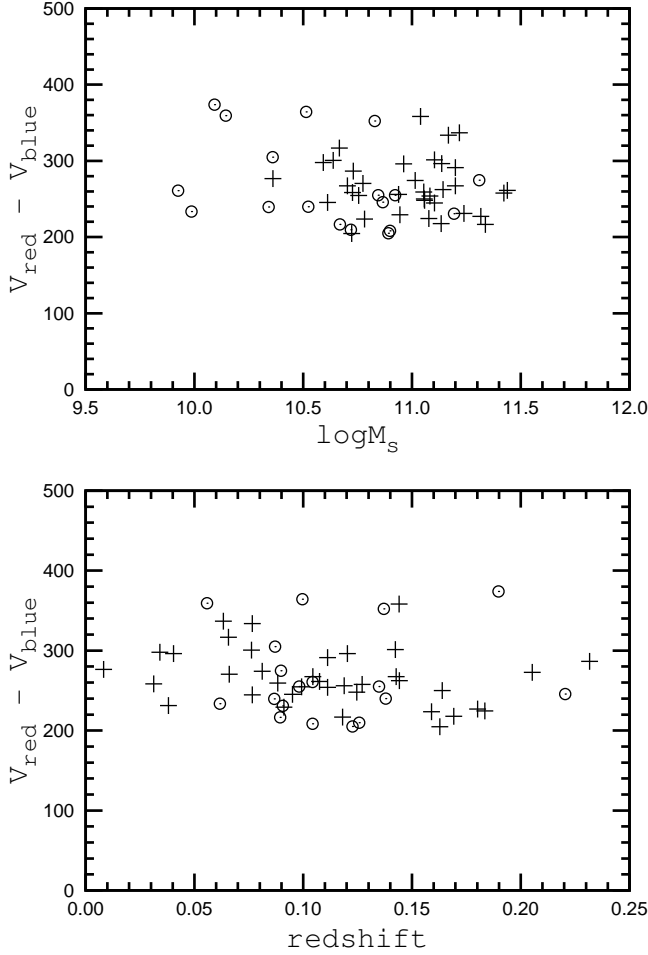


**Figure 3.** The difference between radial velocities of blue  $V_{\text{blue}}$  and red  $V_{\text{red}}$  components (in units of  $\text{km s}^{-1}$ ) as a function of stellar mass of a galaxy (*upper panel*) and of redshift (*lower panel*). The open circles show galaxies from Sample A. The plus signs show galaxies from Sample B.

### 3.2 Velocity separation

Fig. 3 shows the difference between radial velocities of the blue and red components as a function of stellar mass (*upper panel*) and of redshift (*lower panel*). The open circles show galaxies from Sample A, while the plus signs show galaxies from Sample B. The difference between the radial velocities of the blue and red components is determined from the mean value of the differences for individual lines. The scatter is typically a few per cent, but less than 10% in all the cases. Fig. 3 shows that this difference between the radial velocities ranges between  $200 \text{ km s}^{-1}$  and  $400 \text{ km s}^{-1}$ , and that it does not correlate with stellar mass, nor with redshift. However, the upper panel of Fig. 3 shows that the galaxies with AGN-like spectra are more massive, on average, than the galaxies with starburst-like spectra. This agrees with the conclusion by Kauffmann et al. (2003) that AGNs reside almost exclusively in massive galaxies.

Here we will discuss the velocity separations of the double peaks and the Gaussian width parameters of the  $\text{H}\beta$  lines. It was noted above that the only lines that cannot be reliably decomposed into two components are  $[\text{S II}]\lambda 6717$  or/and  $[\text{S II}]\lambda 6731$  while the other lines can be fitted rather well by two Gaussians in 129 selected galaxies. Hence, all 129 galaxies will be included in this particular discussion. The lower-limit difference between the radial velocities of the blue  $V_{\text{blue}}$  and red  $V_{\text{red}}$  components ( $\sim 200 \text{ km s}^{-1}$ )

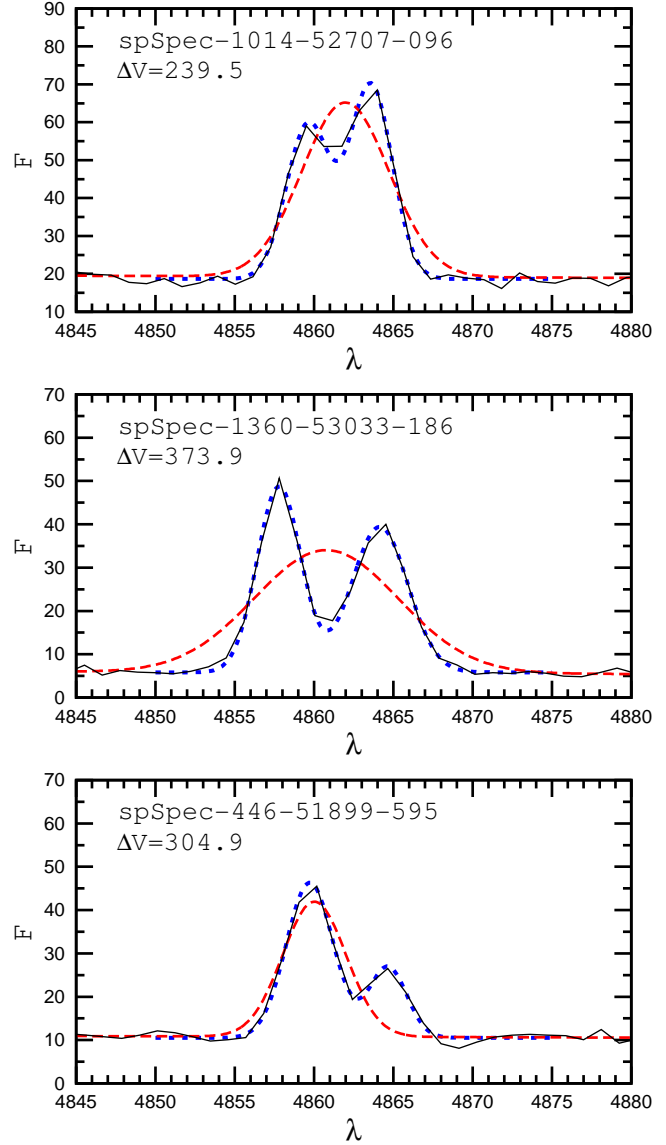


**Figure 4.** The approximation of the observed  $\text{H}\beta$  line profile (dark (black) curve) by the single (long-dashed (red) curve) and two (short-dashed (blue) curve) Gaussians in spectra of three galaxies from Sample A. (A color version of this figure is available in the online version.)

in our sample of galaxies is defined by the requirement that the two peaks in the line profile should be clearly separated. Smith et al. (2010) have selected active galactic nuclei from the SDSS having double-peaked profiles of  $[\text{O II}]\lambda 4959, 5007$  and other narrow emission lines by visual inspection of the quasar spectra. The lower-limit velocity separation of the double peaks in their sample is also around  $200 \text{ km s}^{-1}$ , i.e. similar to that in our sample of galaxies.

The rotation velocity of large spiral galaxies is usually above  $200 \text{ km s}^{-1}$  and can reach about  $300 \text{ km s}^{-1}$  (see the compilation by Pilyugin et al. (2004)). The difference between radial velocities of two  $\text{H II}$  regions in spiral galaxy with large inclination can thus be around  $400 - 600 \text{ km s}^{-1}$ . As an alternative interpretation, the large difference between radial velocities of blue and red components can be parts of two merging systems. The largest difference between radial velocities of the blue and red components ( $\sim 400 \text{ km s}^{-1}$ ) in our sample of galaxies is well within the range given above. One may expect that in case many individual  $\text{H II}$  regions are distributed

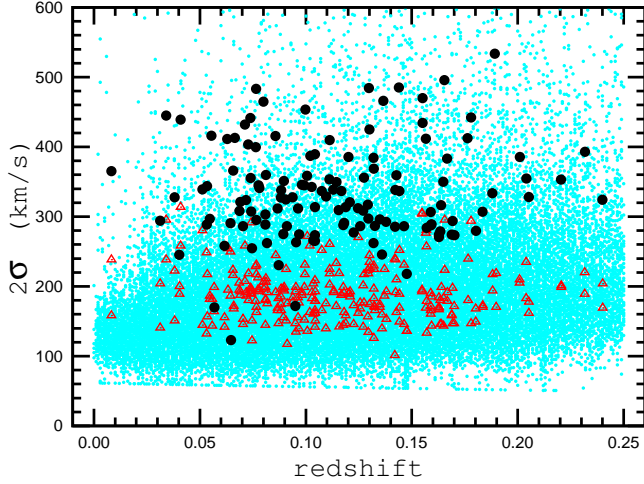


**Figure 5.** The Gaussian width parameter  $\sigma_{H\beta}$  (in units of km/s) as a function of redshift for emission-line galaxies taken from the SDSS (gray (blue) filled circles), for global spectra of the selected 129 SDSS galaxies with double-peaked emission lines (dark (black) filled circles), and for the blue and red components of those galaxies (open (red) triangles). A color version of this figure is available in the online version.

over the disc of a giant spiral galaxy with a large inclination, the emission line profile in the global single-peaked SDSS spectra of such composite nebulae can have a similar width.

### 3.3 Gaussian line width

We have extracted the line width of the  $H\beta$  line ( $\sigma_{H\beta}$ ) for 255,539 emission-line galaxies (with equivalent widths of the  $H\beta$  and  $H\alpha$  lines  $EW(H\beta) > 1.5$ ,  $EW(H\alpha) > 1.5$ , and  $2\sigma_{H\beta} < 600 \text{ km s}^{-1}$ ) from the SDSS database. It should be noted that a single-Gaussian fit to the double-peaked emission line can be bad even as a first-order approximation, Fig. 4.

Fig. 5 shows the Gaussian width parameter  $\sigma_{H\beta}$  (in units of km/s) as a function of redshift for a large sample of emission-line galaxies extracted from the SDSS (gray (blue) filled circles), for the global spectra of the selected 129 SDSS galaxies with double-peaked emission lines (dark (black) filled circles), and for the blue and red components of those galaxies (open (red) triangles). The values of the Gaussian width parameter  $\sigma_{H\beta}$  for the global spectra (including our sample of 129 galaxies) were taken from the SDSS database and measured for the blue and red components. Fig. 5 shows that the line widths of the majority of the blue and red components in our sample of galaxies are within range from  $\sim 140 \text{ km s}^{-1}$  to  $\sim 220 \text{ km s}^{-1}$  and they occupy the same area as the majority of emission-line galaxies from the SDSS. However several components have larger widths, up to  $\sim 300 \text{ km s}^{-1}$ . This suggests that some components can themselves be composite nebulae. The Gaussian width parameters of the global spectra of our sample of galaxies are situated above and along the upper envelope defined by the emission-line galaxies from the SDSS. However, some of them are situated in the same region as the majority of the blue and red components. These are galaxies where the intensities of the blue and red components differ significantly. In such case the single-Gaussian fit to the double-peaked emission line reproduces the strongest component alone as can be seen in the lower panel of Fig. 4. Thus, the large Gaussian width parameters of the global spectra cannot be a reliable criterion for selecting candidates for galaxies with double-peaked emission lines. Using this criterion, one will simply miss

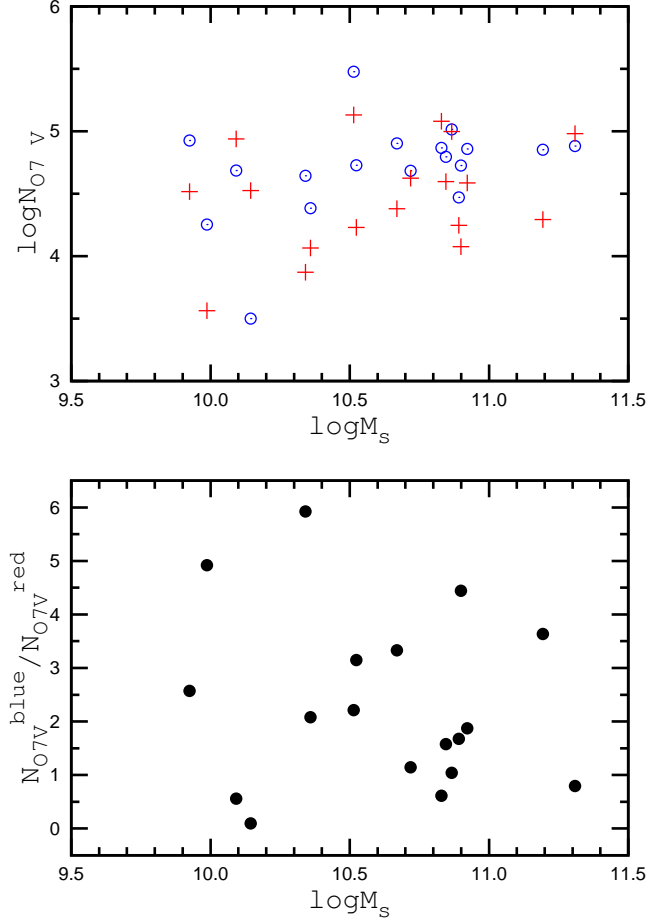


**Figure 6.** *Upper panel.* The equivalent number of O7V stars  $N_{O7V}$  responsible for the excitation of  $H II$  regions versus the host galaxy stellar mass for Sample A. The open (blue) circles show the blue components and the (red) plus signs show the red components. *Lower panel.* The ratio of equivalent numbers of O7V stars responsible for the excitation of the blue and red components. A color version of this figure is available in the online version.

the galaxies where the intensities of the blue and red components differ significantly.

### 3.4 Starburst strength

An important characteristic of a  $H II$  region is the number of the ionising stars it contains. Under the assumption of an ionisation-bounded and dust-free nebula, the  $H\beta$  luminosity provides an estimate of the ionising flux. The ionising flux can be expressed in terms of the number of so-called equivalent O stars of a given subtype responsible for producing the ionising luminosity. The number of zero-age main sequence O7V stars,  $N_{O7V}$ , is usually used to specify the ionising flux. The value of  $N_{O7V}$  can be easily derived from the observed  $H\beta$  luminosity and the Lyman continuum flux of an individual O7V star. The number of ionising photons from an O7V star is  $N_{Lc} = 5.62 \times 10^{48} \text{ s}^{-1}$  (Martins, Schaerer & Hillier 2005) or  $N_{Lc} = 1.12 \times 10^{49} \text{ s}^{-1}$  (Vacca 1994). Here the value of  $N_{Lc}$  after Martins, Schaerer & Hillier (2005) has been adopted. If we instead adopt the value of  $N_{Lc}$  after Vacca (1994) then the number of equivalent O stars are increased by about a factor two. One ionising photon from the star produces 0.157  $H\beta$  photons (0.449  $H\alpha$  photons) from the  $H II$  region (Osterbrock & Ferland 2006). The



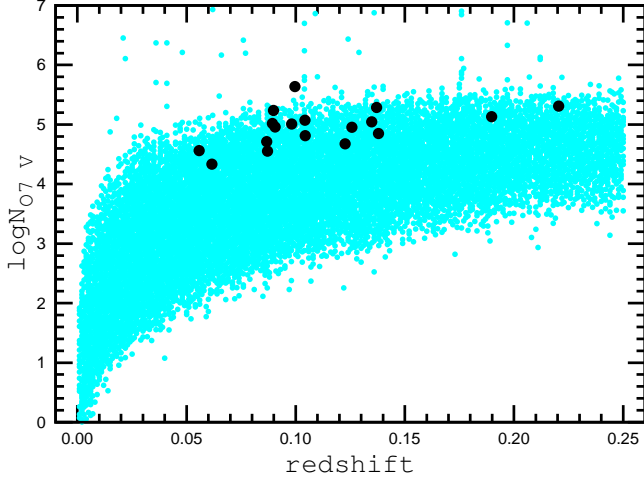


**Figure 7.** The equivalent number of O7V stars  $N_{O7V}$  responsible for the excitation of the H II regions versus redshift for Sample A (dark (black) filled circles) and for star-forming galaxies taken from the SDSS (gray (blue) filled circles). A color version of this figure is available in the online version.

density-bounded dust-free H II region excited by one O7V star will have the H $\beta$  luminosity  $3.38 \times 10^{36}$  erg s $^{-1}$  or  $\log(L_{H\beta}/L_{\odot}) = 2.93$  and the H $\alpha$  luminosity  $7.64 \times 10^{36}$  erg s $^{-1}$  or  $\log(L_{H\alpha}/L_{\odot}) = 3.30$ . When these conditions (density-bounded and/or dust-free) are not met, the values of the number of equivalent O stars obtained here should be interpreted as lower limits.

The reddening-corrected H $\beta$  flux  $F_{H\beta}^O$  is obtained from the observed  $F_{H\beta}^{obs}$  flux using the relation (Blagrave et al. 2007)

$$\log(F_{H\beta}^{obs}/F_{H\beta}^O) = -C_{H\beta}, \quad (12)$$

where  $C(H\beta)$  is the extinction coefficient.

The distances to SDSS galaxies are calculated from

$$d = \frac{cz}{H_0}, \quad (13)$$

where  $d$  is the distance in Mpc,  $c$  the speed of light in km s $^{-1}$ , and  $z$  the redshift.  $H_0$  is the Hubble constant, here assumed to be equal to  $72 (\pm 8)$  km s $^{-1}$  Mpc $^{-1}$  (Freedman et al. 2001). Since objects from Sample A have low redshifts (only two objects have  $z > 0.15$ ) the low-redshift approximation for distance determination has been used.

The upper panel of Fig. 6 shows the equivalent number of O7V stars  $N_{O7V}$  responsible for the excitation of blue and red components in galaxies from Sample A. The lower panel shows the ratio of equivalent numbers of O7V stars responsible for the excitation of blue and red components. Inspection of Fig. 6 shows the typical value of the equivalent number of O7V stars in starbursts in galaxies from Sample A is in the range  $10^4 - 10^5$ . Kennicutt (1988) has given the mean H $\alpha$  fluxes for the three brightest H II regions in a sample of nearby galaxies. Those fluxes, converted to equivalent numbers of O7V stars, correspond to  $N_{O7V} \sim 10^2$ . Thus, both the blue and red components in our sample of SDSS galaxies contain many more (up to 2-3 orders of magnitude) ionising stars, when compared to the brightest H II regions in nearby galaxies. Fig. 7 shows a comparison of the equivalent number of O7V stars  $N_{O7V}$  for Sample A (the sum of the  $N_{O7V}$  for blue and red components) and for a large sample of star-forming galaxies from SDSS. This sample of galaxies were selected from the MPA/JHU catalogs using the dividing line between starburst like objects and AGNs from

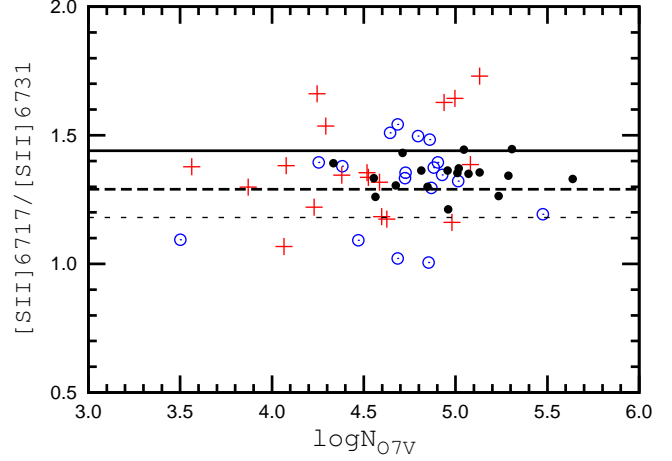


**Figure 8.** The density-sensitive [S II] $\lambda 6717$ /[S II] $\lambda 6731$  line ratio versus the equivalent number of O7V stars  $N_{O7V}$  responsible for the excitation of H II regions. The open (blue) circles show the blue components. The (red) plus signs show the red components. The filled circles show the sum of blue and red components. The solid line shows the zero-density limit ( $N_e = 1$  cm $^{-3}$ ), the dashed line corresponds to the electron density  $N_e = 100$  cm $^{-3}$ , and the dotted line corresponds to the electron density  $N_e = 200$  cm $^{-3}$ . A color version of this figure is available in the online version.

Kauffmann et al. (2003). The reddening-corrected H $\beta$  flux is obtained using Eq.(12). Only the galaxies with  $EW(H\beta) > 1.5$  and  $EW(H\alpha) > 1.5$  are shown. Fig. 7 also shows that the number of ionizing stars in the galaxies with two starbursts from our Sample A are similar to that of galaxies (from the SDSS) with a large amount of ionising stars.

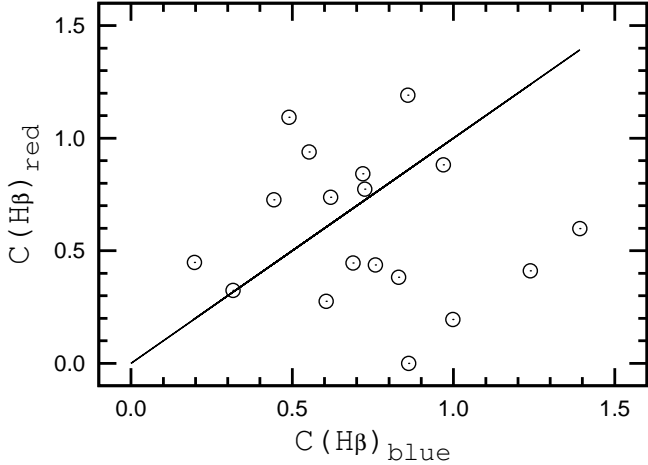
### 3.5 Electron density

Fig. 8 shows the density-sensitive [S II] $\lambda 6717$ /[S II] $\lambda 6731$  line ratio as a function of the equivalent number of O7V stars  $N_{O7V}$  in the starbursts. The open (blue) circles show the blue components. The (red) plus signs show the red components. The filled circles show the data from global spectra (sum of blue and red components). The expected zero density limit ([S II] $\lambda 6717$ /[S II] $\lambda 6731 = 1.44$  at  $N_e = 1$  cm $^{-3}$  with  $t_2 = 1.0$ ), is shown by the solid line. The dashed and dotted lines show the line ratios corresponding to  $N_e = 100$  cm $^{-3}$  ([S II] $\lambda 6717$ /[S II] $\lambda 6731 = 1.29$ ) and  $N_e = 200$  cm $^{-3}$  ([S II] $\lambda 6717$ /[S II] $\lambda 6731 = 1.18$ ), respectively.

The density-sensitive [S II] $\lambda 6717$ /[S II] $\lambda 6731$  line ratio in the global spectra of all galaxies in our Sample A show an electron density  $N_e \leq 200$  cm $^{-3}$  (filled circles in Fig. 8), with the majority of them having  $N_e \leq 100$  cm $^{-3}$ . Hence, they are all in the low-density regime, as is typical for the majority of extragalactic H II regions (Zaritsky, Kennicutt & Huchra 1994; Bresolin et al. 2005; Gutiérrez & Beckman 2010). The [S II] $\lambda 6717$ /[S II] $\lambda 6731$  line ratio in the blue and red components show a larger scatter (see Fig. 8), which may be caused by the uncertainties in the line decomposition.

Two giant H II regions located at different positions inside the disc (one H II regions can be associated with the circumnuclear star formation) may be responsible for the double-peaked emission lines in Sample A. However, the double-peaked emission lines in global spectra can be caused not only by two starbursts in the same galaxy, but also two starbursts in two different galaxies, provided these galaxies are very closely located on the sky (projected on





**Figure 9.** The extinction  $C(H\beta)$  in the blue component versus the extinction  $C(H\beta)$  in the red component for galaxies from Sample A.

top of each other and thus detected within the same SDSS fiber). If the radiation from a star-forming region in a more distant galaxy passes through a less distant galaxy, one may expect that the extinction of the red component (star-forming region in the more distant galaxy) should be larger than the extinction of the blue component (star-forming region in the less distant galaxy). Fig. 9 shows the extinction coefficient  $C(H\beta)$  in the blue component versus the  $C(H\beta)$  in the red component for galaxies in Sample A. Fig. 9 also shows that there is no systematic difference between the values of the extinction coefficient  $C(H\beta)$  in the blue and red components. It should be noted, however, that it cannot be excluded that the more distant galaxies can have slightly lower radial velocities than less distant ones due to the random component of their radial velocities.

#### 4 ABUNDANCES AND TEMPERATURES

It is impossible to divide the  $[O\text{ II}]\lambda 3727 + \lambda 3729$  doublet into a blue and a red component at the SDSS spectral resolution. Therefore, we have used NS-calibration to determine abundances and the  $t_2$  electron temperatures in the blue and red components. The NS-calibration is an empirical calibration for determination of oxygen and nitrogen abundances as well as electron temperatures in H II regions where the nebular oxygen line  $[O\text{ II}]\lambda 3727 + \lambda 3729$  is not available (Pilyugin & Mattsson 2011). The NS-calibration relations express the abundances (and electron temperatures) in terms of the fluxes in the strong emission lines of  $O^{++}$ ,  $N^+$ , and  $S^+$  and have been derived using spectra of H II regions with well-measured electron temperatures as calibration datapoints. The NS-calibration provides reliable oxygen and nitrogen abundances for H II regions of all metallicities. The resultant NS-calibration abundances and electron temperatures are given in Table 1.

The left panels of Fig. 10 show the comparison of oxygen abundances (upper panel), nitrogen abundances (middle panel) and  $t_2$  electron temperatures (lower panel) in the blue components and the same in the red components of galaxies from Sample A. Fig. 10 also shows that the oxygen and nitrogen abundances and  $t_2$  electron temperatures in the blue and red components are close to each other, which may reflect a strong selection effect. Indeed, as it has already been noted above, at the limited SDSS spectral resolution, more or less reliable double-Gaussian fits to the emission lines ( $[III]\lambda 5007$ ,  $[N\text{ II}]\lambda 6584$ ,  $[S\text{ II}]\lambda 6717$  and  $[S\text{ II}]\lambda 6731$ ) can be

obtained if the blue and red components make comparable contributions to the “global lines”. Hence, we have selected spectra with double-peaked emission lines where the intensities of all these lines in the blue and red components are similar and, consequently, the abundances are similar too.

Since the SDSS spectra are closer to global spectra of galaxies rather than to spectra of individual H II regions, the abundances determined from the SDSS spectra are “global abundances”. For our sample of galaxies we can determine the “global flux” in every emission line as the sum of fluxes from the blue and red components, and estimate the global abundances using the NS-calibration. However, as the global flux in the  $[O\text{ II}]\lambda 3727 + \lambda 3729$  doublet can be measured in the spectra considered here, it is possible to estimate the global oxygen and nitrogen abundances and  $t_2$  electron temperatures using another empirical calibration, the ON-calibration (Pilyugin et al. 2010). The ON-calibration relations express the abundances (and electron temperatures) in terms of the fluxes in the strong emission lines  $O^{++}$ ,  $O^+$ , and  $N^+$ . It has also been derived using the spectra of H II regions with well-measured electron temperatures as calibration datapoints.

The resultant global abundances and electron temperatures are given in Table 1. The right panels of Fig. 10 show a comparison of global oxygen abundances (upper panel), nitrogen abundances (middle panel) and  $t_2$  electron temperatures (lower panel) in Sample A determined using the NS- and ON-calibrations. Fig. 10 also shows that the oxygen and nitrogen abundances, as well as the  $t_2$  electron temperatures, derived using the NS- and ON-calibrations are in good agreement, which can be considered as evidence that our abundances and temperatures are realistic.

As it was noted above, the  $[S\text{ II}]\lambda 6717/[S\text{ II}]\lambda 6731$  line ratio in the blue and red components show a larger scatter than that in the global spectra (see Fig. 8), which may be caused by the uncertainties in the line decomposition. How do such uncertainties affect the derived abundances in the blue and red components? We argue it can be estimated in the following way. It is known that the majority of extragalactic H II regions are in the low-density regime (Zaritsky, Kennicutt & Huchra 1994; Bresolin et al. 2005; Gutiérrez & Beckman 2010). The global spectra of all galaxies in our Sample A also show a low electron density having  $N_e \leq 100\text{ cm}^{-3}$  (Fig. 8). Then one can expect that the blue and red components have also a low electron density and, consequently, the  $R_s = [S\text{ II}]\lambda 6717/[S\text{ II}]\lambda 6731$  line ratio in their spectra should be within the interval defined by the  $R_s$  values at  $N_e = 100\text{ cm}^{-3}$  and  $N_e = 1\text{ cm}^{-3}$ .

Let us first assume  $R_s$  at  $N_e = 100\text{ cm}^{-3}$  is the “true” value ( $R_{s,\text{true}}$ ). Then the uncertainties in the line ratio in the blue components can be quantified by the value  $c_b = R_{s,b}/R_{s,\text{true}}$ . If the  $c_b$  is larger/smaller than unity then the flux in the  $[S\text{ II}]\lambda 6717$  line is over-/underestimated by a factor of  $c_{b,1}$  up to  $c_b$  and/or the flux in the  $[S\text{ II}]\lambda 6731$  line is under-/overestimated by a factor of  $c_{b,2}$  up to  $c_b$  so that  $c_{b,1}/c_{b,2} = c_b$ . One can estimate the corrected flux in the sulfur lines as  $(S_2)_{\text{cor}} = [S\text{ II}]\lambda 6717/c_{b,1} + [S\text{ II}]\lambda 6731/c_{b,2}$ . It is evident that the error in the  $S_2$  is maximised when  $c_{b,1} = c_b$  and  $c_{b,2} = 1$  if  $[S\text{ II}]\lambda 6717 > [S\text{ II}]\lambda 6731$  and when  $c_{b,1} = 1$  and  $c_{b,2} = 1/c_b$  if  $[S\text{ II}]\lambda 6717 < [S\text{ II}]\lambda 6731$ . We have then considered the two extreme cases. We have found two values of the corrected flux in the sulfur lines. The uncertainties in this line ratio in the red components can be quantified by the value  $c_r = R_{s,r}/R_{s,\text{true}}$ . The corrected flux  $(S_2)_{\text{cor}}$  in the sulfur lines can be estimated in the same way for the red components. The obtained values of  $c_b$  and  $c_r$  for galaxies in Sample A are all in the range from  $\sim 0.7$  to  $\sim 1.3$ . As a result, the difference between the corrected flux  $(S_2)_{\text{cor}}$  and the observed flux  $(S_2)_{\text{obs}}$  in

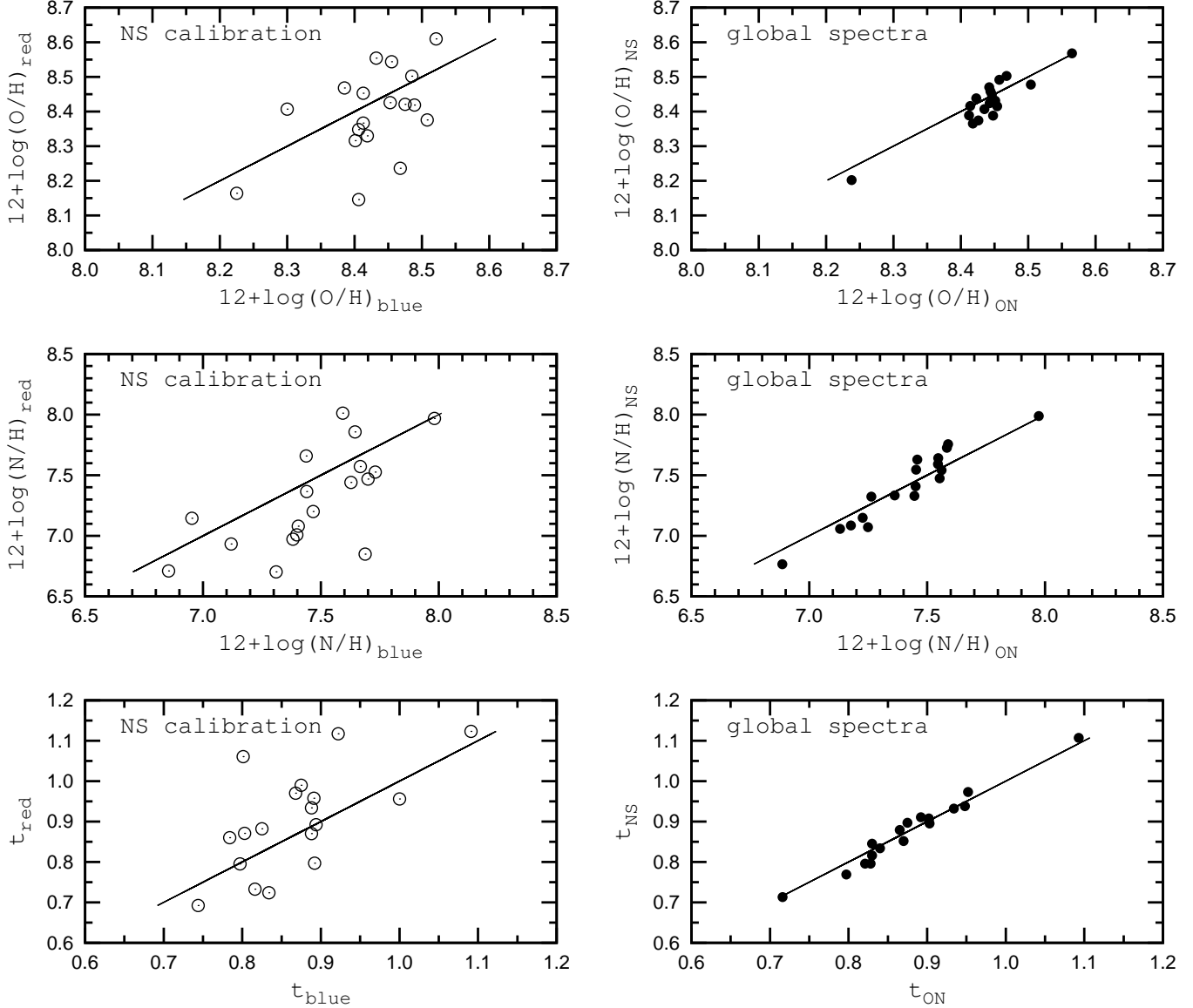


**Figure 10.** *Left column panels.* Comparison of oxygen abundances (upper panel), nitrogen abundances (middle panel) and  $t_2$  electron temperatures (lower panel) in blue components and the same in the red components of the galaxies from Sample A. *Right column panels.* Comparison oxygen abundances (upper panel), nitrogen abundances (middle panel) and  $t_2$  electron temperatures (lower panel) determined from global line fluxes using the NS-calibration with the same derived using the ON-calibration. The solid lines represent equal values.

the sulfur lines is not exceeding  $\sim 15\%$  for any object. We plot the corrected flux  $(S_2)_{\text{cor}}$  against the observed one  $(S_2)_{\text{obs}}$  in the upper panel of Fig. 11 (open (red) circles).

Let us now assume that the  $R_s$  at  $N_e = 1 \text{ cm}^{-3}$  is the “true”  $R_{s,\text{true}}$  value. We plot the corrected flux  $(S_2)_{\text{cor}}$  against the observed one  $(S_2)_{\text{obs}}$  in the upper panel of Fig. 11 (filled (blue) circles). The obtained values of  $c_b$  and  $c_r$  for galaxies in Sample A are again within the range from  $\sim 0.7$  to  $\sim 1.3$  and the difference between the corrected flux  $(S_2)_{\text{cor}}$  and the observed flux  $(S_2)_{\text{obs}}$  in the sulfur lines for blue and red components is never exceeding  $\sim 15\%$ .

One may consider the measured global  $R_{s_g} = [\text{S II}]\lambda 6717/[\text{S II}]\lambda 6731$  as being the “true” value instead of the  $R_s$  at  $N_e = 100 \text{ cm}^{-3}$  and at  $N_e = 1 \text{ cm}^{-3}$ . In such case the differences between the corrected fluxes  $(S_2)_{\text{cor}}$  and flux  $(S_2)_{\text{obs}}$  in the sulfur lines in the blue and red components are usually less than  $\sim 10\%$ .

We have found the corrected oxygen abundances  $(\text{O}/\text{H})_{\text{NS,cor}}$  in blue and red components through the NS-calibration using the values of corrected flux  $(S_2)_{\text{cor}}$  in the sulfur lines. The corrected oxygen abundances  $(\text{O}/\text{H})_{\text{NS,cor}}$  against the observed abundances  $(\text{O}/\text{H})_{\text{NS,obs}}$  are shown in the lower panel of Fig. 11. The lower panel of Fig. 11 shows that the difference between the corrected oxygen abundance  $(\text{O}/\text{H})_{\text{NS,cor}}$  and the observed abundance  $(\text{O}/\text{H})_{\text{NS,obs}}$  is less than 0.03 dex in all cases. This is because the coefficients of the terms with  $\log S_2$  in the NS-calibration relations for oxygen abundance determinations are less than unity for all classes of H II regions (hot, warm and cold) (Pilyugin & Mattsson 2011). Consequently, the uncertainty in  $S_2$  which is less than  $< 15\%$  (or less than  $\sim 0.07$  dex) results in an error in  $\log(\text{O}/\text{H})_{\text{NS,cor}}$  less than 0.03 dex. The difference between the corrected nitrogen abundance  $(\text{N}/\text{H})_{\text{NS,cor}}$  and the observed abundance  $(\text{N}/\text{H})_{\text{NS,obs}}$  is slightly larger, up to 0.07 dex. This is because the coefficients of

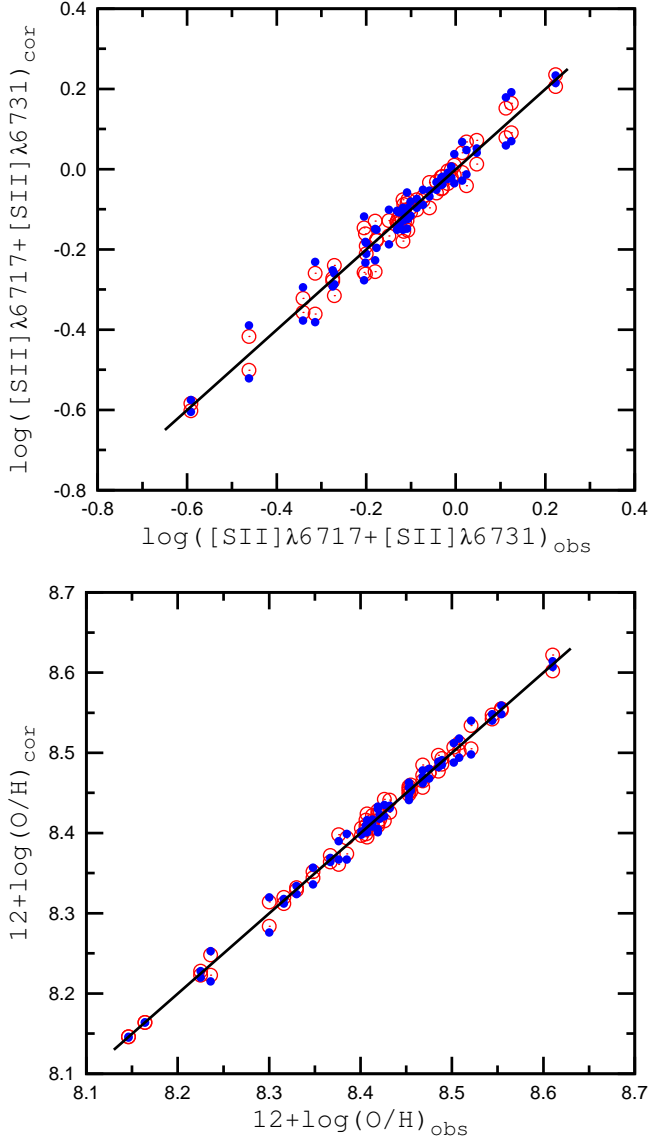


**Figure 11.** *Upper panel.* The corrected flux  $(S_2)_{\text{cor}}$  against the observed flux  $(S_2)_{\text{obs}}$  in the sulfur lines for the blue and red components in the galaxies in Sample A. The open (red) circles show the case when the corrected values have been estimated assuming the “true” line ratio  $[S\text{II}]\lambda 6717/[S\text{II}]\lambda 6731 = 1.44$  which corresponds to the electron density  $N_e = 100\text{ cm}^{-3}$  (see text). The filled (blue) circles show the corrected values obtained assuming the “true” line ratio  $[S\text{II}]\lambda 6717/[S\text{II}]\lambda 6731 = 1.29$  which corresponds to the electron density  $N_e = 1\text{ cm}^{-3}$ . The solid line shows the case of equal values. *Lower panel.* The corrected oxygen abundances  $(\text{O}/\text{H})_{\text{NS,cor}}$  against the observed abundances  $(\text{O}/\text{H})_{\text{NS,obs}}$  in the blue and red components in the galaxies in Sample A. The meaning of the symbols are the same as in the upper panel. The solid line shows the case of equal values. (A color version of this figure is available in the online version.)

the terms with  $\log S_2$  in the NS-calibration relations for nitrogen abundance determinations are close to unity for cold and warm H II regions (Pilyugin & Mattsson 2011). Hence, the given value of the uncertainty in  $S_2$  (up to 15% or up to 0.07 dex) results in a similar error in  $\log(N/\text{H})_{\text{NS,cor}}$ . Thus, the errors in the  $(\text{O}/\text{H})_{\text{NS}}$  and the  $(\text{N}/\text{H})_{\text{NS}}$  abundances caused by the uncertainties in the sulfur line decomposition are relatively small and cannot affect the results significantly.

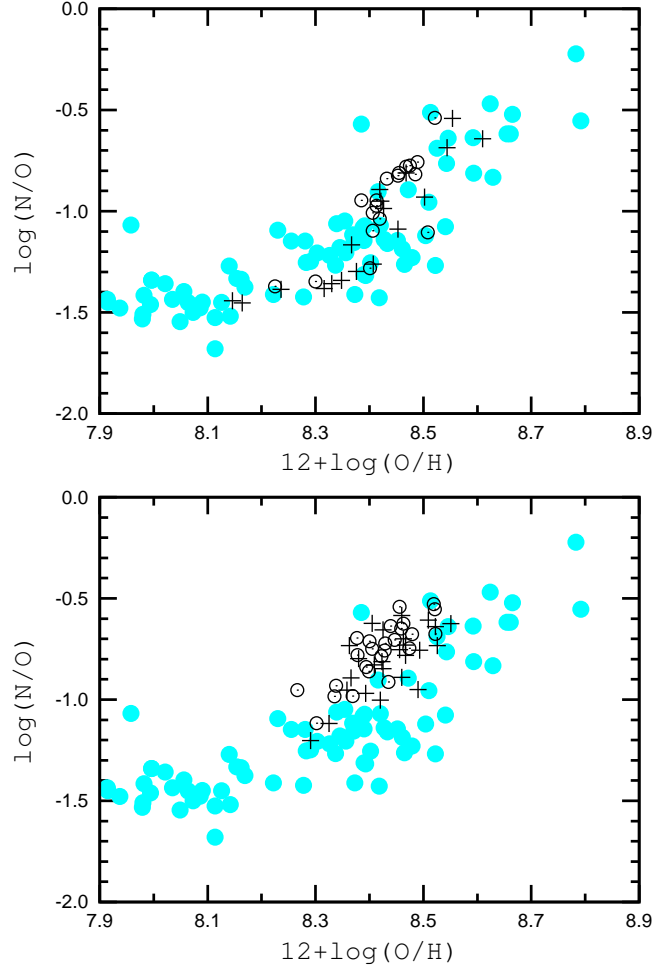


**Figure 12.** The O/H–N/O diagram. *Upper panel.* The open circles show abundances derived using the NS-calibration for blue components of galaxies of the Sample A, the plus signs show that for red components. The filled gray (light-blue) circles show  $T_e$ -based abundances in the sample of best-studied H II regions in nearby galaxies (the compilation of data from Pilyugin et al. (2010)). *Lower panel.* The same as the upper panel but for galaxies which lie in the  $[\text{NII}]\lambda 6584/\text{H}\alpha$  versus  $[\text{OIII}]\lambda 5007/\text{H}\beta$  diagram between the separation lines after (Kauffmann et al. 2003) and after Kewley et al. (2001) (see Fig. 2). (A color version of this figure is available in the online version.)

The O/H–N/O diagram provides an additional possibility to test the correctness of the determined oxygen and nitrogen abundances. The upper panel of Fig. 12 shows the O/H – N/O diagram for Sample A. The open circles show abundances derived using the NS-calibration for blue components, the plus signs show the same for red components. The filled gray (light-blue) circles show  $T_e$ -based abundances in the calibration sample of H II regions in nearby galaxies (the compilation of data from Pilyugin et al. (2010)). Fig. 12 also shows that the abundances derived using the NS-calibration occupy the same region in the O/H – N/O diagram as the  $T_e$ -based abundances of the calibration sample, which implies that our NS-calibration abundances are correct.

The exact location of the dividing line between H II regions and AGNs is still controversial (see, e.g., Kewley et al. 2001; Kauffmann et al. 2003; Stasińska et al. 2006). The objects that lie between the dividing lines according (Kauffmann et al. 2003) and Kewley et al. (2001) in the  $[\text{NII}]\lambda 6584/\text{H}\alpha$  versus  $[\text{OIII}]\lambda 5007/\text{H}\beta$

diagram (see Fig. 2) are starburst like objects if the dividing line according to Kewley et al. (2001) is used but they are AGN-like objects (or, at least, they are not purely thermally photoionised objects) if the dividing line according to Kauffmann et al. (2003) is used. Note, however, that the dividing line suggested by Stasińska et al. (2006) is very similar to that of Kauffmann et al. (2003).

The O/H - N/O diagram may also provide an indirect way to decide which curve [that according to Kauffmann et al. (2003) or that according to Kewley et al. (2001)] outlines best the area occupied by starburst-like objects in the BPT diagram. If objects that lie between these lines are starburst-like objects, the emission line fluxes in their spectra correspond to thermally photoionised objects. The NS-calibration (and other strong-line calibrations) developed for thermally photoionised nebulae will then provide reliable oxygen and nitrogen abundances for these objects, which will occupy the same region in the O/H - N/O diagram as H II regions in nearby galaxies. If, on the other hand, the [N II] fluxes are produced by non-thermal radiation or at least are enhanced by the contribution of non-thermal radiation, using the NS-calibration on these nebulae will result in too high nitrogen abundances. One may expect that the positions in the O/H - N/O diagram will be shifted significantly as compared to the positions of thermally photoionised H II regions in nearby galaxies. The lower panel of Fig. 12 shows the O/H - N/O diagram for galaxies which lie between the two dividing lines in the [N II]  $\lambda 6584/H\alpha$  versus [O III]  $\lambda 5007/H\beta$  diagram together with the positions of thermally photoionised H II regions in nearby galaxies. The positions of the galaxies considered here show a systematic shift toward higher N/O-ratio compared to the positions of the thermally photoionised H II regions in nearby galaxies, which suggest that the emission lines are distorted by the contribution of non-thermal radiation, i.e. they are not purely thermal photoionisation objects. If this is the case, the line according to (Kauffmann et al. 2003) is to be favoured as it outlines the area occupied by certainly starburst-like objects in the BPT diagram. It has been assumed (e.g., by Juneau et al. 2011) that the line from Kewley et al. (2001) can be considered as the curve outlining the area occupied by “pure” AGNs in the BPT diagram, and that objects which lie between the curves according to Kauffmann et al. (2003) and Kewley et al. (2001) are composite objects where both a starburst and an AGN make contributions. However, this interpretation is not indisputable (Cid Fernandes et al. 2010, 2011).

Comparison of oxygen abundances in the blue and red components and the global oxygen abundances tell us something about how representative/correct the abundances derived from the global spectra are. Fig. 13 shows the difference between oxygen abundances in the blue component and the global oxygen abundances versus the difference between oxygen abundances in the red component and the global oxygen abundances for galaxies in Sample A. Furthermore, Fig. 13 clearly shows that there is an anti-correlation between the two abundance differences described above. This means the global oxygen abundance obtained using the NS-calibration is typically in between the oxygen abundance of the blue and red components.

## 5 CONCLUSIONS

We have extracted several hundred galaxies from the SDSS spectral database with double-peaked emission lines in their global spectra. Among other possibilities (e.g. double-peaked AGNs), one may expect such line profiles if two strong starbursts take place si-

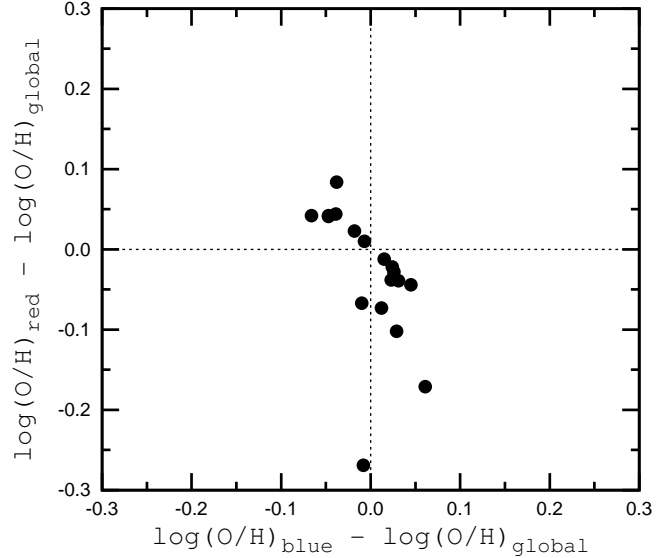


**Figure 13.** The difference between oxygen abundances in the blue component and the global oxygen abundances versus the difference between oxygen abundances in the red component and the global oxygen abundances for galaxies in Sample A.

multaneously in a galaxy. We have fitted the emission lines ( $H\alpha$ ,  $H\beta$ , [O III]  $\lambda 5007$ , [N II]  $\lambda 6584$ , [S II]  $\lambda 6717$  and [S II]  $\lambda 6731$ ) by two Gaussians in 129 spectra to separate the flux of the two (blue and red) components. A more or less reliable decomposition of the emission lines has been found for 55 spectra.

Using the standard classification [N II]  $\lambda 6584/H\alpha$  versus [O III]  $\lambda 5007/H\beta$  diagram and the dividing lines after Kauffmann et al. (2003), we have divided the galaxies from our sample into two subsamples: a Sample A consisting of 18 galaxies where both components belong to the photoionised objects and a Sample B containing 37 galaxies which show nonthermal ionisation (AGN). All blue and red components have narrow lines regardless of their positions in the [N II]  $\lambda 6584/H\alpha$  versus [O III]  $\lambda 5007/H\beta$  diagram.

The differences between radial velocities of the blue and red components lie between 200 and 400 km s<sup>-1</sup> for both subsamples. The equivalent number of ionising stars is within the range  $10^4 - 10^5$  O7V stars for each component in Sample A.

We have estimated the oxygen and nitrogen abundances as well as the electron temperatures for each component, and for the global spectra in Sample A, using the recent NS-calibration. We have found that the global oxygen abundance is typically in between the oxygen abundance of the blue and red components. This conclusion is based on a small sample of galaxies which, by selection, have red and blue line components of similar flux. To confirm (or reject) our conclusion a larger sample of galaxies should be considered. Applying the ON-calibration on the global spectra shows that the ON-calibration and NS-calibration give oxygen and nitrogen abundances and electron temperatures which are in good agreement.

The O/H - N/O diagram for the galaxies in our sample gives indirect evidence suggesting that the dividing line in the [N II]  $\lambda 6584/H\alpha$  versus [O III]  $\lambda 5007/H\beta$  diagram from Kauffmann et al. (2003) outlines well the area occupied by starburst-like objects.

We find also that two giant H II regions located at different positions inside the disc (one H II region may be associated with cir-

cumnuclear star formation) seem to be responsible for the double-peaked emission lines in the spectra of Sample A. However, two starbursts in two different galaxies which are projected on top of each other, as alternative scenario for the origin of the double-peaked emission lines, cannot be excluded. Photometric and spectroscopic observations with higher resolution may help to resolve this issue.

## ACKNOWLEDGMENTS

L.S.P. and I.A.Z. acknowledge support from the Cosmomicrophysics project of the National Academy of Sciences of Ukraine. Part of this work was supported by the Spanish Plan Nacional de Astronomía y Astrofísica under grants AYA2008-06311-C02-01, AYA2007-67965-C03-02 and AYA2010-21887-C04-01.

Funding for the SDSS and SDSS-II has been provided by the Alfred P. Sloan Foundation, the Participating Institutions, the National Science Foundation, the U.S. Department of Energy, the National Aeronautics and Space Administration, the Japanese Monbukagakusho, the Max Planck Society, and the Higher Education Funding Council for England. The SDSS Web Site is <http://www.sdss.org/>.

The SDSS is managed by the Astrophysical Research Consortium for the Participating Institutions. The Participating Institutions are the American Museum of Natural History, Astrophysical Institute Potsdam, University of Basel, University of Cambridge, Case Western Reserve University, University of Chicago, Drexel University, Fermilab, the Institute for Advanced Study, the Japan Participation Group, Johns Hopkins University, the Joint Institute for Nuclear Astrophysics, the Kavli Institute for Particle Astrophysics and Cosmology, the Korean Scientist Group, the Chinese Academy of Sciences (LAMOST), Los Alamos National Laboratory, the Max-Planck-Institute for Astronomy (MPIA), the Max-Planck-Institute for Astrophysics (MPA), New Mexico State University, Ohio State University, University of Pittsburgh, University of Portsmouth, Princeton University, the United States Naval Observatory, and the University of Washington.

## REFERENCES

- Abazajian K.N., et al. 2009, *ApJS*, 182, 543  
 Baldwin J.A., Phillips M.M., & Terlevich R. 1981, *PASP*, 93, 5  
 Blagrove K.P.M., Martin P.G., Rubin R.H., Dufour R.J., Baldwin J.A., Hester J.J., & Walter D.K. 2007, *ApJ*, 655, 299  
 Bresolin F., Schaerer D., González Delgado R.M., & Stasińska G., 2005, *A&A*, 441, 981  
 Brinchmann J., Charlot S., White S.D.M., Tremonti C., Kauffmann G., Heckman T., & Brinkmann J. 2004, *MNRAS*, 351, 1151  
 Cid Fernandes R., Stasińska G., Schlickmann M.S., Mateus A., Asari N.V., Schoenell W., Sodr   L. 2010, *MNRAS*, 403, 1036  
 Cid Fernandes R., Stasińska G., Schlickmann M.S., Mateus A., Asari N.V., Schoenell W., Sodr   L. 2011, *MNRAS*, 413, 1687  
 Freedman W.L., Madore B.F., Gibson B.K., et al., 2001, *ApJ*, 553, 47  
 Guti  rrez L., & Beckman J.E. 2010, *ApJ*, 710, L44  
 Izotov, Y.I., Thuan, T.X., & Lipovetsky, V.A. 1994, *ApJ*, 435, 647  
 Izotov Y.I., Stasińska G., Guseva N.G., & Thuan T.X. 2004, *A&A*, 415, 87  
 Juneau S., Diskinson M., Alexander D.M., Salim S. 2011, *ApJ*, 736, 104  
 Kauffmann G., Heckman T.M., Tremonti C., et al. 2003, *MNRAS*, 346, 1055  
 Kennicutt R.C., 1988, *ApJ*, 334, 144  
 Kewley L.J., Dopita M.A., Sutherland R.S., Heisler C.A., & Trevena J. 2001 *ApJ*, 556, 121  
 Kniazev A.Y., Pustilnik S.A., Grebel E.K., Lee H., & Pramskij A.G. 2004, *ApJSS*, 153, 429  
 Markwardt, C.B., 2009, in *Astronomical Society of the Pacific Conference Series*, Vol. 411, D. Bohlender, D. Durand, & P. Dowler, ed., *Data Analysis Software and Systems XVIII*, ASP Conference Series, p.251  
 Martins F., Schaerer D., & Hillier D.J., 2005, *A&A*, 436, 1049  
 Osterbrock D.E., & Ferland G.J. 2006, *Astrophysics of gaseous nebulae and active galactic nuclei*, 2nd edn., University Science Books, Sausalito, CA  
 Pilyugin L.S., & Mattsson L. 2011, *MNRAS*, 412, 1145  
 Pilyugin L.S., & Thuan T.X. 2007, *ApJ*, 669, 2007  
 Pilyugin L.S., & Thuan T.X. 2011, *ApJ*, 726, L23  
 Pilyugin L.S., V  lchez J.M., Cedr  s B. & Thuan T.X. 2010, *MNRAS*, 403, 896  
 Pilyugin L.S., V  lchez J.M., & Contini T. 2004, *A&A*, 425, 849  
 Pilyugin L.S., V  lchez J.M., & Thuan T.X. 2010, *ApJ*, 720, 1738  
 Smith K.L., Shields G.A., Bonning E.W., McMullen C.C., Rosario D.J., & Salviander S. 2010, *ApJ*, 716, 866  
 Stasi  nska, G., Cid Fernandes, R., Mateus, A., Sodr  , L., & Asari, N.V. 2006, *MNRAS*, 371, 972  
 Storey P.J., & Zeippen C.J. 2000, *MNRAS*, 312, 813  
 Thuan T.X., Pilyugin L.S., & Zinchenko I.A. 2010, *ApJ*, 712, 1029  
 Tremonti C.A., Heckman T.M., Kauffmann G., et al. 2004, *ApJ*, 613, 898  
 Vacca W.D. 1994, *ApJ*, 421, 140  
 York D.G., Anderson J.E., Anderson S.F., et al. 2000, *AJ*, 120, 1579  
 Zaritsky D., Kennicutt R.C., & Huchra J.P., 1994, *ApJ*, 420, 87